

Elastoplastic and Polymorphic Transformations in Iron Films Loaded by Ultrashort Laser Shock Waves

S. A. Murzov^{a,b,*}, S. I. Ashitkov^b, E. V. Struleva^b, P. S. Komarov^b, V. A. Khokhlov^c,
V. V. Zhakhovskii^{a,b,c}, and N. A. Inogamov^{c,b,a}

^a *Dukhov Research Institute of Automatics, Moscow, 127055 Russia*

^b *Joint Institute for High Temperatures, Russian Academy of Sciences, Moscow, 125412 Russia*

^c *Landau Institute for Theoretical Physics, Russian Academy of Sciences, Chernogolovka, Moscow oblast, 142432 Russia*

**e-mail: murzovs@gmail.com*

Received October 19, 2021; revised October 19, 2021; accepted October 21, 2021

Abstract—The results of experimental studies of the laser shock waves initiated by a picosecond pulse in iron are presented. Experimental measurements are processed and analyzed using theoretical approaches and numerical simulation. Interest in picosecond actions is caused by uniquely high strain rates, in particular, the dependence of the thresholds of elastoplastic and polymorphic transformations on the strain rate. Investigations are necessary for the development of the field of laser hardening of metals. The first steps in this direction have been taken, although this kind of approach to laser forging hardening is already widely used in practice. Modern developments in the field of shock wave generation and their experimental diagnostics are used, and the related methods of theoretical interpretation of experimental data are being developed. The difficulty lies in the picosecond time scale, since the diagnostics of experiments is limited by kinematics, namely, measuring the coordinates of the free surface. To elucidate the polymorphic transformation kinetics on picosecond time scales, the technique of inverse analysis of the free surface velocity is used for the first time. This technique is validated using the results of hydrodynamic and molecular dynamics simulation with direct extraction of mechanical stresses and strains. A theoretical study of reconstructed free surface velocity profiles by traditional methods confirms the results obtained in the field of their applicability, specifically, on elastic and plastic shock wave fronts. The transformation of iron into the ϵ phase takes place in the initial region of shock wave propagation, as long as a shock wave has a sufficient amplitude. The cause is a pressure limitation of 40 GPa because of optical breakdown in glass and shock wave attenuation during wave propagation.

DOI: 10.1134/S1063776122030098

1. INTRODUCTION

The first information about the use of high-power nanosecond lasers for studying condensed matter equations of state is given in [1, 2]. Mechanical phenomena appear during any laser action. In particular, lasers are shock wave (SW) generators, which compete with the mechanical methods of creating SWs in a condensed phase using a collision of a target with a flyer plate or using explosives.

A relatively new scientific and technological trend is associated with the use of ultrashort femto- and picosecond laser pulses to study the behavior of condensed media at high strain rates. Such pulsed light sources are created when chirped pulses are amplified.

Two important features, namely, thermomechanical and mechanical, are related to ultrashort actions. The zone in which energy absorption and heating of a substance occur is quite thin; therefore, it is necessary to take into account the excess of the electron temperature over the lattice temperature [3]. Although we have experience in formulating such models [4–8], the

SW generation in iron has the following specific features.

The first feature consists in a thermomechanical effect. The motion of the main heated layer mass begins after the end of laser heating. The thermal expansion of the substance from a heated film layer creates compression waves in a glass substrate and inside an iron film, although the heated layer causes compression wave generation in the case of a long-time pulse [5, 9–11]. Compression waves travel far away from the heated layer, and heat remains accumulated in the heated layer substance; entropic and acoustic modes are said to be separated.

The second feature consists in the long time of the compressed state of a condensed medium in a compression wave. A compression wave forms during the acoustic decay of a high-pressure layer. The behavior of materials under the action of extremely short mechanical loads with a change to unloading is beyond microsecond and even nanosecond actions.

The use of such actions is interesting for studying the picosecond kinetics of the decomposition of molecules, e.g., in explosives [12, 13]. Even greater interest is shown in the study of the kinetics of elastoplastic and polymorphic transformations in a solid phase [6, 14–28]. The experimental [14–18] and calculation [6, 23–27] studies demonstrate a sharp increase in the thresholds separating elastic and plastic shock-wave flows. As a result, a theoretical explanation was given for a series of brilliant femtosecond experiments performed by American scientists [29–32]: SWs propagate significantly faster than they should at a given pressure amplitude.

In applications, the problem arises in connection with promising modern technologies of picosecond laser forging [33–35]. Another important new direction is related to picosecond diagnostics of objects with a complex internal structure [36, 37]. Acoustic vibrations are excited by an ultrashort action to be measured using a series of picosecond probe pulses with a small time difference, and an internal structure is restored using an elastic vibration spectrum. Unlike laser forging, energetically weak actions (nondestructive control) are used for excitation and probing. Elastic surface waves [38–40] were used in [36, 37]. Crack control is traditionally carried out using Rayleigh and Lamb surface waves. The novelty of works [36, 37, 40] consists in the extreme miniaturization of measurements.

The authors of [20, 41, 42] began to study of the influence of the rate of loading on the kinetics and completion of the complex polymorphic transformation $\alpha \rightarrow \epsilon$ in iron. This work is a continuation of such studies. The stress at which transition to a plastic motion mode occurs is known to increase the loading speed. For many crystalline bodies, this dependence is sharply enhanced when the rate of deformation exceeds $10^3\text{--}10^4\text{ s}^{-1}$, which is interpreted as a consequence of a change in the mechanism of dislocation motion from thermal fluctuation to over-barrier one controlled by phonon friction [43].

A picosecond mechanical load makes it possible to achieve metastable states of matter far from equilibrium and to study the behavior of various materials at extremely high strain rates [44]. In particular, in the picosecond time range, the authors of [14–22, 44, 45] were able to come close to the maximum possible (“ideal”) bulk and shear strength for a number of metals.

Currently, polymorphic transitions in a microsecond SW loading range have been detected in many metals, semiconductors, and ionic compounds [46]. The behavior of iron and steel, which are the main structural materials of power engineering and mechanical engineering, under extreme conditions has been actively studied over the past few decades. At present, the following four solid phases of iron are known [47]: α (bcc), γ (fcc), δ (bcc), and ϵ (hcp).

The phase polymorphic transition $\alpha \rightarrow \epsilon$ in iron was detected using an inflection point in a Hugoniot adiabat [48]. This transition was studied in detail in SW experiments in a submicrosecond loading range [49–52], and it is accompanied by a change in the magnetic properties. At a pressure of 13 GPa, iron undergoes the $\alpha \rightarrow \epsilon$ polymorphic transformation into the high-pressure ϵ phase. The SW profile in [21, 49–53] has a three-wave configuration. The first wave is an elastic precursor, which corresponds to the yield strength (approximately 0.5 GPa for submicrosecond loading), followed by the front of a plastic SW in the α phase. In the third jump, densification occurs due to the $\alpha \rightarrow \epsilon$ transformation. The reverse phase transition to the α phase during unloading appears at a pressure below 13 GPa, which leads to a hysteresis of the loading–unloading curve.

Laser methods using pico- and femtosecond optical pulses are applied to generate extremely short (about 0.1 ns) shock loads [14–22]. Diagnostics is performed by an interferometric pumping–probing method with a chirped probe pulse [15, 16, 20, 54], which makes it possible to measure the surface displacement in a subnanosecond range at a time resolution of 1 ps.

The first experiments on determining the metastable compressibility of iron during a picosecond impact action were performed in [20]. The metastable elastic compression adiabat was estimated using the results of measurements on 250- and 540-nm-thick iron film samples (0.999 purity). The detected maximum stress behind the elastic precursor front reached 27 GPa at a propagation length of 250 nm. The maximum shear stress was 7.9 GPa, which is higher than the strength obtained by ab initio calculations [55, 56] and can be explained by an increase in the shear modulus.

The free surface velocity profiles of thicker iron film samples 1.2 and 1.4 μm thick were measured in [21]. The interpretation of the free surface velocity profiles was based on the reconstruction of state curves in the stress–strain ($\sigma\text{--}V/V_0$) variables. Transformation into the ϵ phase occurs at a pressure above 25 GPa, which is about twice as high as that reached upon microsecond loading. A three-wave structure was not detected because of a relatively low rate of plastic relaxation.

Microsecond actions were considered in [57–60] and loading with a pulse duration of 200 ps was considered in [21].

The pulse duration in our work was 1.2 ps, which is two orders of magnitude shorter than that in [21]. We consider a similar experimental formulation: an iron film on a glass substrate, which is irradiated by a laser pulse through the substrate. To reconstruct the stress and strain evolution of the material in the $\sigma\text{--}V/V_0$ plane during wave passage, we use the technique of inverse analysis of the free surface velocity. This technique has long been developed [57, 58]. We used it tak-

ing into account the unloading part of the curve, which allowed us to observe a partial polymorphic phase transformation. A piecewise quasi-stationary approximation was used to restore the stress and the strain in the film of the smallest thickness; that is, the SW velocity in a sample was assumed to be constant along the path length equal to the smallest thickness of an available experimental set. The inverse analysis technique was validated using the results of molecular dynamics simulation. The mechanical action of a laser pulse in molecular dynamics is based on a two-temperature hydrodynamic calculation with allowance for the absorption of laser radiation by an iron film on a substrate.

2. EXPERIMENTAL SCHEME AND MEASUREMENT TECHNIQUE

The motion of the rear surface of the iron film samples at the exit of SW was measured by spectral interferometry [54] using chirped pulses during a single laser action.

A pumping laser pulse was focused on a film metal sample through a glass substrate, and SW phenomena were detected on the rear free surface using a frequency-modulated probe pulse (Fig. 1).

The source of the pump and probe pulses was a femtosecond titanium-sapphire laser system assembled according to a chirped pulse amplification circuit. 40-fs pulses at a central wavelength of 795 nm with a spectrum width of ± 30 nm, which were generated by master oscillator 1, were sent to a time expander, or stretcher 2, where they were further converted into frequency-modulated 300-ps pulses. These pulses were then amplified in amplifier 3, which consisted of a regenerative amplifier and a two-pass power amplifier. After the regenerative amplifier, part of the chirped pulse was redirected from the optical path and used for diagnostics. The rest of the radiation after the power amplifier was directed to time compressor 4, where it was compressed to the desired duration, and was then used as pumping pulses.

The pumping radiation was focused on the surface of film sample 5 (see inset to Fig. 1) through transparent substrate 6 with a lens with a focal length of 20 cm into a spot with a spatial Gaussian distribution with $r_0 = 30 \mu\text{m}$.

This spot size provided almost uniaxial compression of the micron-thick target material (the spot size was much larger than the target thickness). The pulse energy was smoothly varied using polarization attenuator 7 and was controlled by calibrated photodiode 8. After each laser pulse, the target was moved approximately 200 μm to a new location using micromanipulator 9.

This experimental configuration (heating through a glass plate) brings about a limited incident laser radiation intensity because of possible appearance of non-

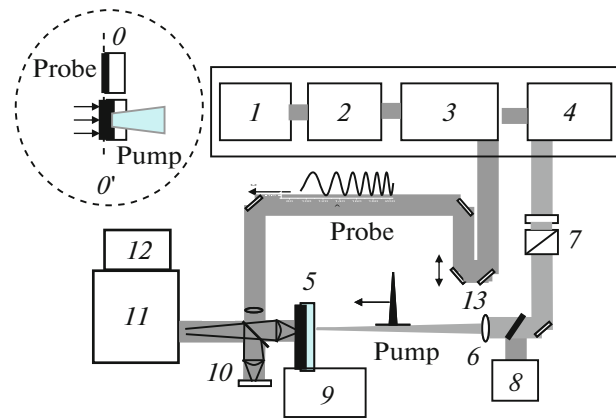


Fig. 1. Optical measurement scheme: (1) master oscillator, (2) stretcher, (3) amplifier, (4) compressor, (5) film sample, (6) lens, (7) polarizing attenuator, (8) photodiode, (9) micromanipulator, (10) Michelson interferometer, (11) diffraction spectrometer, (12) CCD camera, and (13) optical delay line.

linear effects and optical breakdown in the glass. To decrease the peak intensity, the duration of a heating pulse was increased from 40 fs to 1.2 ps by adjusting the laser system compressor. In the experiments, the laser pulse energy was $E = 100 \pm 5 \mu\text{J}$, which corresponds to the incident energy density at the center of the focal spot $F_0 = 3.4 \text{ J/cm}^2$. The pulse energy in the experiments was specially selected to generate maximum-amplitude compression pulses in studied samples. Exceeding this energy E led to the distortion of a detected spatial displacement profile and to a decrease in the free surface velocity due to the development of optical breakdown and radiation absorption in the substrate glass.

To diagnose the displacement dynamics $z(t)$ of the rear free surface of the metallic sample at the exit of a compression SW, we used Michelson interferometer 10, which was assembled according to the image transfer scheme (Linnik configuration) and was combined with Ecton-2300i diffraction spectrometer (Cherny-Turner scheme) 11 with a diffraction grating of 600 grooves/mm. The image transfer was carried out using an Olympus objective microlens with a numerical aperture $\text{NA} = 0.3$, which provided a spatial resolution of 2 μm in the target plane. Optical signals at the exit from the spectrometer were detected with Sensi-Cam QE CCD camera 12 with a cooled 12-bit matrix 1375×1375 pixels in size. Optical delay line 13 served to correct the delay time between heating and probe pulses on adjusting the circuit or changing samples. The applied optical scheme ensured monitoring of the process dynamics at a time resolution $\delta t \approx 1 \text{ ps}$ in the time interval $\Delta t = 0-200 \text{ ps}$.

The experimental samples were armco-iron films 480, 580, 740, 970, and 1160 nm thick deposited by magnetron sputtering onto 150- μm -thick glass sub-

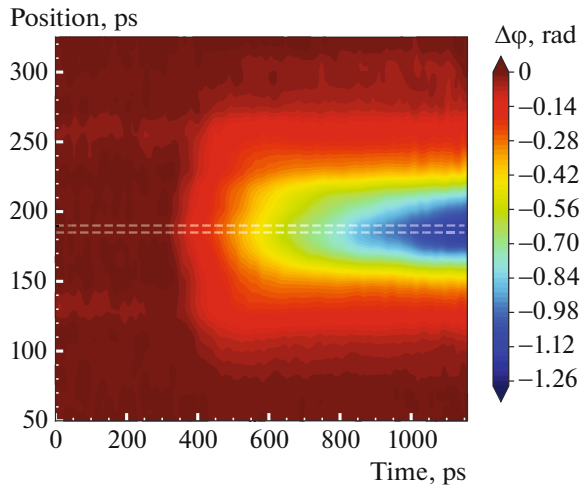


Fig. 2. Space–time distribution of the probe pulse phase when SW reaches the rear surface of a 970-nm-thick iron sample. The displacement profile $z(t)$ is constructed for the area between the dashed lines. The scales along the ordinate and abscissa axes were calculated by converting the matrix pixels into measures of length ($0.4 \mu\text{m}/\text{pixel}$) and time ($0.167 \text{ ps}/\text{pixel}$). The color scale is given in radians.

strates. An armco-iron plate of 0.95 purity was used as a magnetron target. The sample thickness was measured in the laser action area using a Veeco Multimode 5 atomic force microscope with an accuracy of $\pm 5 \text{ nm}$.

In the experiments, the free surface of the samples of different thicknesses was positioned with a micro-manipulator 9 (see Fig. 1) into the object plane OO' of the interferometer objective lens (see inset to Fig. 1) with an accuracy not worse than $2 \mu\text{m}$. The adjustment was carried out according to the maximum contrast of the interference fringes. The accuracy of setting a general (relative) time measurement scale on changing samples with different film thicknesses was less than 100 fs , which was significantly shorter than the time resolution of the measurements. This error consists of the difference in the substrate thicknesses and the positioning accuracy of the sample surface and, in total, does not exceed $10\text{--}20 \mu\text{m}$. Dividing the thickness error by the velocity of light, we determine the specified inaccuracy (100 fs). For the given set of film thicknesses, the difference in the times of reaching the rear surface is several tens of picoseconds. Therefore, the error of measuring the difference in the SW exit times that is related to the positioning accuracy and the difference in the sample thicknesses may be neglected.

To determine a zero time reference, we used an additional 20-nm-thick film sample similarly to [29]. This sample thickness is comparable with the laser radiation absorption depth in iron. The pulse energy is absorbed by conduction electrons and then transferred to the lattice within the electron–phonon heat exchange time of about 1 ps [61]; then, the rear surface

of the film begins to move. Note that similar processes of radiation absorption and heating of the lattice take place when a laser irradiates other samples. Thus, the beginning of displacement of the 20-nm-thick film can be taken as the zero time reference $t_0 = 0$. This time scale is associated with the absolute time of compression pulse motion from a heating zone to the free surface in each film. The accuracy of determining time t_0 was estimated at $\pm 1 \text{ ps}$.

To process data, we used Fourier analysis of interferograms, which included their comparison and allowed us to restore the space–time distribution of the change in the amplitude ($\Delta A(y, t)$) and phase ($\Delta\phi(y, t)$) of the diagnostic reflected wave (here y is the spatial coordinate along the spectrometer slit). The surface displacement Δz is related to the phase change as

$$\Delta z = \lambda \Delta\phi / 4\pi. \quad (1)$$

The following three interferograms were recorded in each experiment: the interferogram of the sample surface before irradiation (initial); when SW reached the surface (temporary); and after the end of the process, i.e., a few seconds after irradiation (final). A comparison of the initial and temporary interferograms provides information about the space–time dynamics of the SW process.

As an example, Fig. 2 shows the space–time distribution of diagnostic wave phase $\Delta\phi(y, t)$, which describes the dynamics of the spatially inhomogeneous motion of the rear free surface of an iron film sample of thickness $h = 970 \text{ nm}$ when SW generated by laser radiation with $E = 100 \mu\text{J}$ reaches the surface. An example of processing the experimental data is presented in Fig. 3.

Profiles were constructed for the central part of the irradiation zone with integration over a spatial interval of $\pm 2 \mu\text{m}$, which corresponded to the incident radiation energy density range $\Delta F/F_0 = 0.01$. Figure 3 shows the displacement and velocity profiles of the free rear surface of a 970-nm-thick sample after the arrival of SW. The surface displacement (black curve) was calculated directly from the phase shift from the experimentally measured phase distribution $\Delta\phi(y, t)$ in Fig. 2. The resulting surface velocity profile (Fig. 3, yellow curve) was obtained by differentiating the displacement profile (gray curve) followed by smoothing and iterative processing, ensuring the best correspondence of the velocity integral (red curve) to the measured profile $z(t)$.

Thus, the applied measurement scheme provided monitoring of the sample surface displacement $\Delta z = \Delta z(t)$ as a function of time at a spatial resolution $\delta y \approx 2 \mu\text{m}$ along the radial coordinate in the target plane and at a time resolution $\delta t = 1 \text{ ps}$ in the time interval $0\text{--}200 \text{ ps}$ determined by the spectrometer dispersion. The applied Fourier analysis of two-dimensional interferograms [62] with the normalization of phase

distributions ensures the error of measuring the phase shift of a diagnostic pulse at a level $\delta\psi \approx 0.01$ rad, which corresponds to the error of determining the surface displacement at a level $\delta z \leq 1-2$ nm.

3. INVERSE ANALYSIS OF KINEMATIC DATA

3.1. From Kinematics to Dynamics and Internal States of the Medium

After initial processing, we obtained kinematic information, namely, free surface velocity history $u_{fs}(t)$ in experiments with different film thicknesses. Several approaches to constructing a theoretical description are possible. SW profiles can be analytically described. The researcher extracts information about the time of arrival of SW and characteristic inflection points and, assuming that a certain physical effect could occur in the substance, interprets experimental results in terms of model concepts about elastoplastic and polymorphic transformations.

Another approach is direct numerical simulation. This approach is used when it is difficult to analytically take into account the influence of the parameters of a physical model. As a result of a series of calculations, the model parameters are chosen and a conclusion is made about its applicability by comparing calculated $u_{fs}(t)$ profiles with experiment data. Here, a physical model can be based on the properties of the substance to be studied, which are known a priori and do not depend on an experiment explicitly. Since it can be difficult to develop a model, simplified phenomenological models are used to achieve agreement between experimental and calculated data.

The purpose of such phenomenological models is to approximately describe a complex physical phenomenon, e.g., the kinetics of a phase transition, fracture, or chemical reactions in a complex microcrystalline structure of a material. The variation of the parameters of such models is based only on a description of an experiment, which makes it possible to achieve the ultimate goal, namely, agreement between calculated and experimental data. This approach was successfully used in [53] to simulate the polymorphic $\alpha \rightarrow \epsilon$ phase transformation in iron during a microsecond action.

The ultrashort effects on a metal with a polymorphic phase transformation considered in this work complicate the formulation of a physical model such as those mentioned above. First, a model should cover radiation absorption and two-temperature (2T) physics, namely, electron-ion relaxation and heat propagation through the electron subsystem from an absorption layer. Second, a model of coordinated thermal and dynamic parts of the problem describes the conversion of femtosecond heating into pressure. For this purpose, a system of 2T equations, which is given in [63], is constructed. As a result, the equations and the thermodynamic state of the medium where

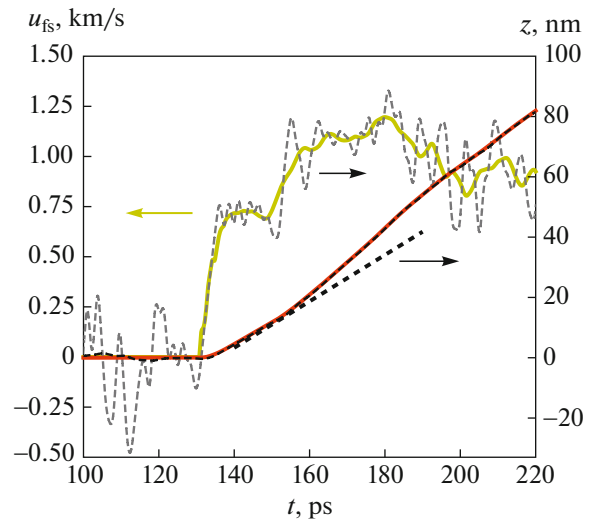


Fig. 3. (gray dashed line) Result of numerical differentiation of the free surface displacement $z(t)$ measured experimentally. (yellow curve) The final surface velocity profile $u_{fs}(t)$ of a 970-nm-thick iron film sample was obtained by numerical differentiation followed by smoothing of (dashed black curve) experimentally detected displacement $z(t)$. Iteration procedure ensures the best correspondence of the integral of the smoothed velocity profile (red curve) to the measured $z(t)$ profile.

pressure initiates SW motion are applied in the hydrostatic approximation. Third, the SW leaves the laser melting zone, and its further propagation occurs in a solid phase. Therefore, the SW propagation in an iron film should be calculated for a deformed solid body with allowance for the presence of a polymorphic phase transformation.

An approach is proposed to obtain data on density $\rho(h, t)$ and longitudinal stress $\sigma(h, t)$. To this end, we approximate a $u_{fs}(h, t)$ function using experimental results obtained for various film thicknesses. This approach requires experiments for at least two [21] or three [59] different film thicknesses depending on the order of the approximating polynomials. We use a piecewise linear approximation of the velocity; therefore, the approximation of only the first derivative of the free surface velocity is embedded in the model. Since the initial data are the time profiles of the free surface coordinates, the use of a higher-order approximation would mean the approximation of the third derivative of the quantity to be measured. Knowing the values of ρ and σ and the shock Hugoniot of elastic compression and plastic compression in the α and ϵ phases, we can determine the phase state of a solid body.

3.2. Method of Interpretation of Experimental Data

Aidun and Gupta [57] proposed and the authors of [21, 59, 60] improved a method for reconstructing stress and strain profiles using experimental free

boundary velocity profiles $u_{fs}(t)$ in samples of different thicknesses. The technique is based on reconstructing of a function of the free surface velocity of two variables, $u_{fs}(t, h)$, namely, time t and Lagrangian coordinate h . Each free surface velocity profile is an $u_{fs}(t)$ dependence for a given iron film thickness h . The relation $u_{fs} = 2u$ is used for the transition from the free surface velocity to mass velocity u (i.e., the velocity of Lagrangian particles). The relation is valid in the linear acoustics approximation, as long as the pressure is much lower than the bulk compression modulus of the material (170 GPa in iron). As a result, we have a set of profiles measured at a high time resolution but for several sample thicknesses (e.g., for two thicknesses [21]). We have information about the time dependence of the free surface velocity for five different film thicknesses to be used to construct a model.

To calculate longitudinal stress σ and strain $\mu \equiv 1 - V/V_0$, it is necessary to integrate the following equation of motion of a substance in a certain limited experimental data region:

$$\frac{\partial \mu}{\partial t} = \frac{\partial u}{\partial h}, \quad (2)$$

$$\frac{\partial \sigma}{\partial h} = -\rho_0 \frac{\partial u}{\partial t}. \quad (3)$$

To determine the stress at time (t_1, h_1) , it is necessary to integrate the derivative $\partial u / \partial t$ with respect to h from boundary point h_b ,

$$\sigma(t_1, h_1) - \sigma(t_1, h_b) = -\rho_0 \int_{h_b}^{h_1} \frac{\partial u}{\partial t}(h, t_1) dh. \quad (4)$$

To calculate the strain at time (t_1, h_1) , the partial derivative $\partial u / \partial h$ is integrated over time with respect to variable t from boundary point t_b ,

$$\mu(t_1, h_1) - \mu(t_b, h_1) = - \int_{t_b}^{t_1} \frac{\partial u}{\partial h}(h_1, t) dt. \quad (5)$$

The integration is performed from boundary $t_b(h)$ or $h_b(t)$, where $\sigma = 0$ and $\mu = 0$ are the states before the arrival of SW. The second point is chosen on a profile, namely, t_1 or h_1 . Setting the boundary conditions gives an insight into the domain of definition, where function $u(h, t)$ takes nonzero values. Here, we have only a finite set of experimental profiles for a very limited set of films (five different thicknesses) but at a relatively high time resolution, $\Delta t \approx 1$ ps.

3.3. Technique of Integration of Kinematic Relations

We use the following simplified form of velocity approximation, discarding the quadratic term in contrast to [59]:

$$u(h, t) = \frac{u_i(h)[t_{i+1}(h) - t] - u_{i+1}(h)[t - t_i(h)]}{t_{i+1}(h) - t_i(h)}, \quad (6)$$

where $t_i(h) < t < t_{i+1}(h)$. In Eq. (6), $t_i(h)$ and $u_i(h)$ are functions of h , which are determined by piecewise linear interpolation and cubic spline on experimental profiles, respectively. Subscripts i correspond to different reference points selected on each $u_{fs}(t)$ profile manually. The points are connected to each other by a piecewise linear function. Time points are increasing, $t_i(h) > t_{i-1}(h)$, with subscript i . Function $h_i(t)$ denotes the inverse function of $t_i(h)$.

The method errors are an important characteristic due to a small number of profiles for different h and the freedom of choosing reference points on a profile; therefore, they are studied, e.g., in [59], where the method error was found to reach its maximum for the smallest and largest film thicknesses. In this work, the partial derivatives in Eqs. (4) and (5) are approximated by finite differences, and the integration is performed numerically, unlike, e.g., [57, 59], where the calculation is carried out using an analytically specified piecewise function $u(h, t)$, the antiderivatives of which are calculated in advance for each individual interval of integration. For internal points, the central difference

$$\frac{u(h + \Delta h, t) - u(h - \Delta h, t)}{2\Delta h}$$

is applied.

For the points near the boundary of the domain of definition, the derivative

$$\frac{\partial u}{\partial h} \approx \frac{\Delta u}{\Delta h} \quad (7)$$

is approximated by a directional finite difference except for the case with the minimum film thickness,

$$\frac{u(h_s, t) - u(h_s - \Delta h, t)}{\Delta h},$$

$$\frac{u(h_l + \Delta h, t) - u(h_l, t)}{\Delta h},$$

where h_s and h_l belong to the boundary of the computational domain, $\Delta h = (h_l - h_s)/N$, $N = 300$ is the number chosen to achieve convergence during integration. One of the features of the methods for integrating the system of Eqs. (2) and (3) of kinematic relations, in contrast to classical approaches (wave arrival time and the jump in the mass velocity at a known sample thickness are detected), is that stress and strain diagrams depend only on the relative location of the velocity profiles of the free surface in samples of different thicknesses on the time axis. In other words, the stress–strain diagram is invariant with respect to shifts in the wave arrival time in all experiments or to an increase in all film thicknesses by the same value. In the case of a film with the smallest thickness, we propose to use the absolute wave arrival time and the free surface velocity in the elastic precursor (point 2 in Fig. 4 for the profile of film with $h = 480$ nm). In this case, the wave is assumed to move at an average con-

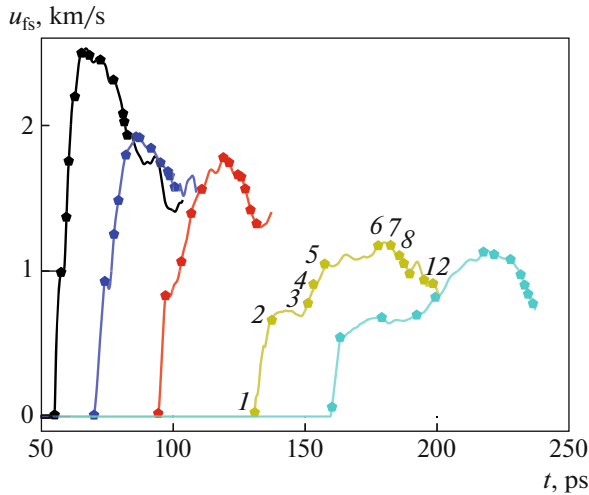


Fig. 4. Free surface velocity profiles for films of 480, 580, 740, 970, and 1160 nm thick (from left to right). Twelve characteristic points were selected on each profile to approximate experimental dependences in the reverse analysis of a series of profiles.

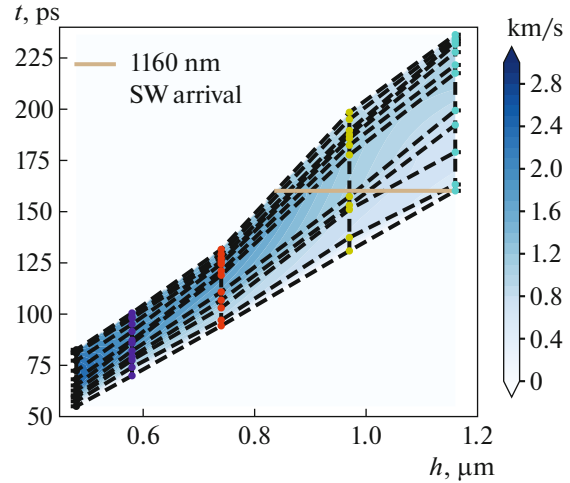


Fig. 5. Functions $t_i(h)$ are set as a piecewise linear interpolation and are constructed using the reference points from Fig. 4. The coloring corresponds to the free surface velocity $u_{fs}(h, t)$. The circles indicate the positions of the reference points, and their color corresponds to the curves in Fig. 4.

stant velocity $U_{sl} = h_1/t_2(h_1)$, where $t_2(h_1)$ is the time corresponding to point 2 on the profile of the thinnest film ($h_1 = 480$ nm). As a result, we can estimate the derivative of Eq. (7),

$$\frac{\partial u}{\partial h} \approx \frac{\partial u}{\partial t} U_{sl}^{-1}. \quad (8)$$

Similarly, expressions for the partial time derivative are calculated,

$$\frac{\partial u}{\partial t} \approx \frac{\Delta u}{\Delta t}. \quad (9)$$

The time step is $\Delta t(h) = [t_f(h) - t_s(h)]/N$, where the difference between the first ($t_s(h)$) and the last ($t_f(h)$) reference points on the $u_{fs}(t)$ profile for a given thickness is set; that is, the step depends on sec. Due to the integration over thickness h in Eq. (4), it is also necessary to determine the dependence on it, as is shown in Fig. 5.

3.4. Reliability of the Technique from Comparison with Numerical Simulation

$\sigma-V/V_0$ diagrams are compared to substantiate the reliability of the proposed procedure. In one case, the stresses and densities are extracted directly from molecular dynamics (MD) simulation, which is used as a source of complete information about the mechanical and thermodynamic states of a group of Lagrangian coordinates (i.e., the initial particle positions) at $h = 150, 160, 200, 250, 300, 350, 400, 450, 500, 550,$ and 600 nm. In another case, the stresses and strains are calculated only using information about the time dependences of the velocities of all Lagrangian particles, which are shown in Fig. 6. Here,

the integration of laws of conservation is based on a two-dimensional interpolation of the time dependences of the velocities of these particles (Fig. 7).

The initial stage of the process is modeled using 2T hydrodynamics. During short laser pulses, the temperature of the electrons absorbing laser radiation can significantly exceed the temperature of the ion subsystem. Hydrodynamic modeling is used to perform a complete calculation of the absorption of a laser pulse, which is associated with the processes of electron-ion relaxation and heat conduction. At the times longer than the electron-electron and ion-ion relaxation times, the electron and ion subsystems have specific quasi-equilibrium temperatures T_e and T_i , respectively [3]. The 2T stage time, during which $T_e \gg T_i$ and which is determined by the electron-ion relaxation rate, can be significantly longer due to the large difference in the electron and ion masses. At a sufficiently high laser pulse energy, substance motion becomes noticeable already at the 2T stage, which makes it necessary to consider the thermal problem together with the equations of motion in terms of general 2T hydrodynamics [64]. The system of equations of 2T hydrodynamics has the form [65, 66]

$$\begin{aligned} \frac{\partial x(x^0, t)}{\partial t} &= u(x^0, t), & \frac{\rho \partial x(x^0, t)}{\partial x^0} &= \rho_0, \\ \frac{\partial u(x^0, t)}{\partial t} &= -\frac{\partial P(x^0, t)}{\rho^0 \partial x^0}, & P &= P_e + P_i, \end{aligned}$$

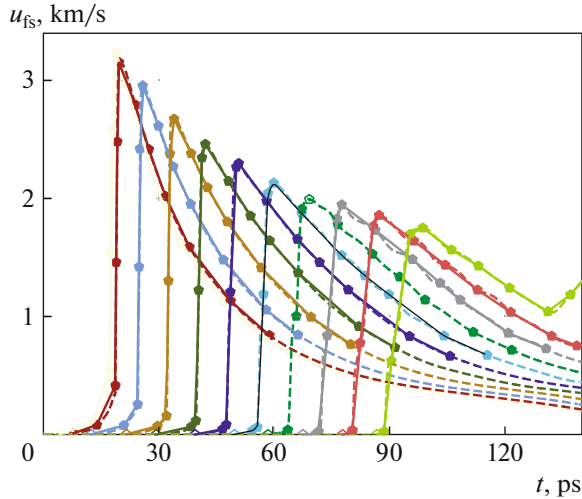


Fig. 6. History of the double velocity of Lagrangian particles due to MD simulation with initial positions of 150, 160, 200, and 600 nm (from left to right). The points are connected by a piecewise linear function, which is used to approximate the function $u(h, t)$ and is illustrated by solid lines. The dashed lines are plotted using the initial data of MD simulation.

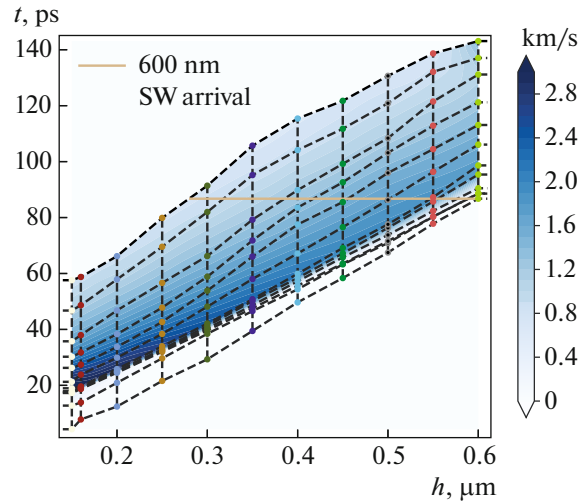


Fig. 7. Functions $t_i(h)$ are set as a piecewise linear interpolation and are constructed using the reference points from Fig. 6. The coloring corresponds to the free surface velocity $u_{fs}(h, t)$. The circles indicate the positions of the reference points, and their color corresponds to the curves in Fig. 6.

$$\begin{aligned} \frac{\partial E_e(x^0, t)}{\partial t} &= \frac{\partial}{\rho^0 \partial x^0} \left(\frac{\kappa_e \rho \partial T_e}{\rho^0 \partial x^0} \right) - Q_{ei} \\ &+ \frac{Q(x^0, t)}{\rho} - P_e \frac{\partial u}{\rho^0 \partial x^0}, \\ \frac{\partial E_i(x^0, t)}{\partial t} &= Q_{ei} - P_i \frac{\partial u}{\rho^0 \partial x^0}, \\ Q_{ei} &= \alpha(T_e - T_i), \end{aligned}$$

where E_e , E_i , and α are the specific (per unit mass) electron and ion energies and the electron–ion heat exchange coefficient, respectively, and κ_e is the electron thermal conductivity. At a constant initial density ρ^0 , initial coordinate x^0 can be used as a Lagrangian variable. The system is closed by the equations of state (EOS) of substance and material models of the thermal conductivity and the electron–ion heat exchange. Ionic (phonon) thermal conductivity is absent, since it is negligible compared to the electronic one. The target to be irradiated consists of iron and glass on which it is deposited. Since they have significantly different densities, it is necessary to specify either a larger initial cell length in glass (inversely proportional to the ratio of the glass and iron densities) or different masses in cells (in proportion to the initial density) in a Lagrangian description. We used the second approach, which gives a more accurate description of motion in glass.

The picture of the resulting compression wave is characterized by the presence of a heating layer related to heat conduction, on the one hand, and an advanced SW, on the other. The SW is ahead of the heat conduction wave at a depth of 500 nm. We extract the velocity

profile of a Lagrangian particle as a function of time and use this profile in an MD calculation when an iron sample is under the action of a mobile potential barrier with the same time dependence of the velocity. Thus, the effect of laser SW penetrating into an iron film is simulated.

To describe the ion subsystem (without the contribution of the electron subsystem) of iron (P_i , E_i), we used the tabulated wide-range EOS for α iron in the solid state, which was set up Khishchenko on the basis of works [67–69].

For the electron subsystem of iron (EOS, thermal conductivity, electron–ion heat exchange coefficient), we used analytical formulas derived by analyzing the results of density functional theory (DFT) calculations with the VASP package. We also applied the analytical formulas constructed by Petrov for transition metals [70].

There are no free electrons in glass, $P_e = 0$ and $E_e = 0$; that is, single-temperature hydrodynamics is used. Khishchenko’s caloric EOS (Mie–Grüneisen type) is used. The initial density in glass is $\rho_0 = \rho_{0, \text{glass}} = 2.2 \text{ g/cm}^3$.

During the action of a laser pulse, the substance displacement is very small. The heat source Q describing the absorption of laser radiation in iron with $x^0 > 0$ can be taken in its simplest form with a spatial profile frozen into the substance (depending only on x^0),

$$Q(x^0 > 0, t) = \frac{F_{\text{abs}}}{\sqrt{\pi} d_{\text{skin}} \tau} \exp \left[-\frac{x^0}{d_{\text{skin}}} - \left(\frac{t}{\tau} \right)^2 \right]. \quad (10)$$

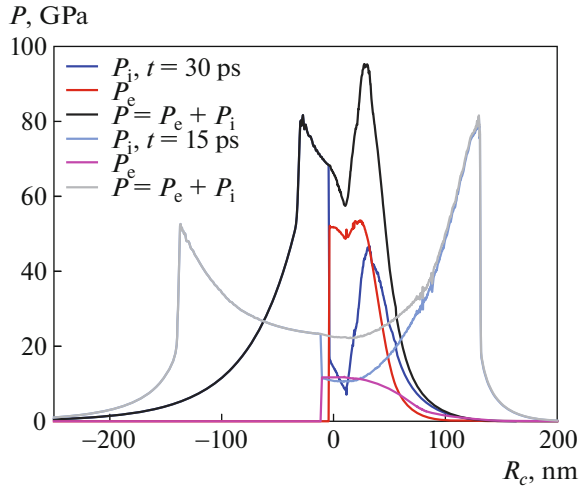


Fig. 8. Pressure profiles near the iron–glass boundary at times of 3 and 15 ps as functions of the distance from this boundary R_c . For iron, the ionic (P_i), electronic (P_e), and total ($P = P_i + P_e$) pressures are presented. Only total pressure $P = P_i$ exists in glass and electronic contribution is absent.

Here, for iron, F_{abs} is the absorbed fluence, d_{skin} is the skin depth (absorption depth), and τ is the pulse duration. Time t is measured from the maximum of the pulse.

The quantity of absorbed heat was calculated on using experimental data and qualitative–empirical relations. The quantitative estimation of the absorbed energy density as a function of incident energy F_0 is determined by the absorption coefficient in iron [71], and it is 1.1 mJ/cm². Then the energy is divided between an iron plate and glass. On the assumption that a breakdown occurred at the iron–glass interface and hot electrons from the metal transferred part of the heat to the glass, the fractions of absorbed energy in the metal and in the glass are determined from the best coincidence of the calculated and experimental free surface velocity profiles in a 160-nm-thick iron film. In the calculations, we took $F_{\text{abs}} = 400$ mJ/cm², $d_{\text{skin}} = 15$ nm, and $\tau = 0.5$ ps.

The heating of glass with $x^0 < 0$ was modeled by heat source Q in the form

$$Q(x^0 < 0, t) = \frac{F_{\text{glass}}}{\sqrt{\pi} d_{\text{glass}} \tau} \exp\left[\frac{x^0}{d_{\text{glass}}} - \left(\frac{t}{\tau}\right)^2\right], \quad (11)$$

where $F_{\text{glass}} = 700$ mJ/cm² is the absorbed fluence and $d_{\text{glass}} = 50$ nm is the skin depth.

As an example, Fig. 8 shows the characteristic pressure profiles at the end of the 2T stage (3 ps) and at the time when the contribution of the electronic component decreases (15 ps).

The calculation in MD simulation uses information about the Lagrangian node velocity at a depth of

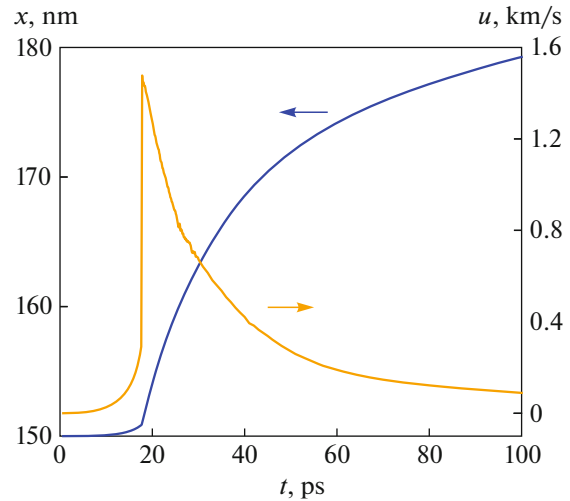


Fig. 9. Coordinate x and velocity u of a Lagrangian node with an initial coordinate $x = 150$ nm.

150 nm, which was obtained by hydrodynamic 2T modeling of the absorption of a laser pulse by a thin film on a glass substrate. Figure 9 shows the position and velocity of this node in time.

MD simulation is carried out for a sample $600 \times 60 \times 10$ nm in size and consists of a periodically repeated polycrystalline $600 \times 60 \times 10$ nm structure multiplied 10 times along the axis of propagation of an ultrashort pulse. At the left boundary, a potential barrier, which moves according to the law that repeats the history of particle motion in the 2T-hydrodynamics calculation, begins to act on the sample at the initial time. The MD simulation results were processed to extract the evolution history of a group of Lagrangian particles. Lagrangian particles are 0.25-nm-wide sections of one-dimensional profiles along the wave propagation axis.

The approximation of function $u(h, t)$ is shown above in Fig. 7 with separated nodal points and the grayscale corresponding to the free surface velocity. The method reproduces the stresses and strains determined in the MD calculation. Figure 10a shows shock Hugoniots of the elastic and plastic α phase, adiabats of the ϵ phase, and the adiabat of the ϵ phase calculated at the given MD potential. Figure 10b depicts the time dependences of the longitudinal stress for various Lagrangian particles. The last time for which the stress history can be restored is limited to the time of SW arrival at a Lagrangian particle with the maximum initial coordinate.

Figure 10c displays the distribution maps of the local order parameters of atoms Q_4 and Q_6 [72, 73]. To visualize an atomic structure, only the parameter of central symmetry could be used in MD [74]. However, there is a problem in determining different crystal structures, which is associated with the potential energy fluctuations of atoms increasing with tempera-

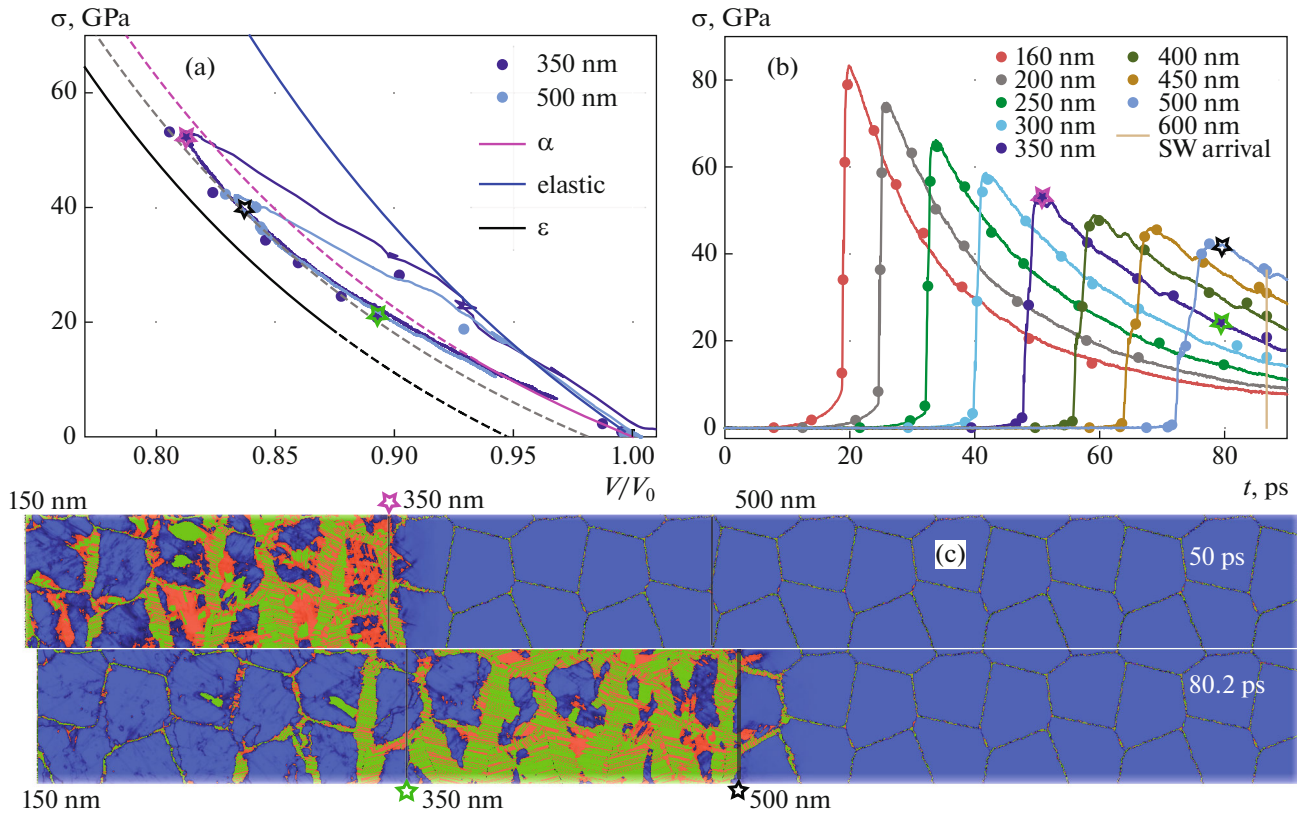


Fig. 10. (a) Calculation of phase curve $\sigma-V/V_0$ using kinematic MD simulation relationships for films 350 and 500 nm thick. The points reconstructed by the inverse analysis technique are located near solid lines of the same color, which corresponds to the MD calculations. The shock Hugoniot of various iron phases are illustrated by solid (in stable phase) and dashed (in metastable phase) lines. The adiabat of the ϵ phase of iron in MD simulation is shown by the dashed gray line. (b) Reconstructed stress profiles in time for Lagrangian particles with various initial coordinates. (c) Symmetry parameter distribution maps [74]. Blue, red, and green correspond to the α , γ , and ϵ phases of iron, respectively. The asterisks indicate the positions of Lagrangian particles with coordinates 350 and 500 nm at times of 50 and 80.2 ps. The left edge of the sample is controlled by the motion of a Lagrangian particle with a coordinate of 150 nm taken from hydrodynamic modeling (see Section 2.4).

ture. The advantage of this method for determining a crystal structure [71, 72] is a weak temperature dependence and independence from density in combination with low computational complexity.

For an isolated atom, Q_{lm} functions in the spherical coordinate system depend only on the angles characterizing the radius vector $\mathbf{r}_{ij} = \mathbf{r}_j - \mathbf{r}_i$ between a pair of atoms. The average over the neighboring atoms in the environment of the isolated atom is calculated as follows:

$$\bar{Q}_{lm}(i) = \langle Y_{lm}(\theta(\mathbf{r}_{ij}), \phi(\mathbf{r}_{ij})) \rangle, \quad (12)$$

$$Q_l^2 = \frac{4\pi}{2l+1} \sum_{m=-l}^l |\bar{Q}_{lm}|^2, \quad (13)$$

where Y_{lm} are the spherical harmonics and θ and ϕ are the polar and azimuthal angles of the spherical coordinate system for vector \mathbf{r}_{ij} , respectively. The averaging is performed over neighboring atoms, which are neighbors in a local Voronoi diagram. A local order parameter is invariant with respect to the orientation

of the coordinate system and the rotation transformations of the system of atoms, which is square Q_l in Eq. (13). Moreover, the order parameters for which $l = 4$ and 6 give different types of crystal lattice at high temperatures as well [75].

A coordinate in the Q_4 - Q_6 plane determines the coloring of the crystalline phases of iron in Fig. 10c, including that at the temperatures such that the regions of possible values of parameters Q_4 and Q_6 can overlap for different types of crystal lattices. The bcc phase is characterized by values

$$Q_4^{\text{bcc}} = 0.03636965, \quad Q_6^{\text{bcc}} = 0.5106882;$$

for an ideal crystal with the hcp phase, we have

$$Q_4^{\text{hcp}} = 0.09722222, \quad Q_6^{\text{hcp}} = 0.4847617;$$

for the fcc phase, we have

$$Q_4^{\text{fcc}} = 0.1909407, \quad Q_6^{\text{fcc}} = 0.5745243.$$

The closeness of fcc and hcp structures makes it difficult to distinguish them; however, the coexistence

of both the ϵ and γ phases of iron was experimentally observed during short laser pulses [76]. To distinguish phases on the plane in the Q_4 – Q_6 coordinates, we determined the boundaries of values for each phase and a condition for the value of central symmetry parameter C_S [74]. Testing according to the condition $C_S < 2.5$ makes it possible to determine whether a certain substance is a crystal or a liquid phase. The cubic and hexagonal lattices are separated by the threshold value of the central symmetry parameter $C_S > 4.9$. If the lattice is cubic, a pixel on the map is colored according to hcc at $Q_4 > Q_4^{\text{hcp}}$; otherwise, it is colored according to fcc.

3.5. Calculations Using Kinematic Relations

We apply the described technique to calculating σ – V/V_0 diagrams using the experimental data for the free surface velocity $u_{fs}(t)$. The first step is to approximate the function $u_{fs}(h, t)$. It is advisable to choose reference points corresponding to physically identical inflection points on velocity profile curves for different values of h , which makes the assumption that there is the same number of such features on the curves. Although, in the absence of, e.g., a pronounced elastic precursor, it is possible to introduce a larger number of points into the approximation of the plastic wave front.

Figure 4 shows the selection of a set of points, namely, 12 points from each profile, a total of 5 profiles. As a result, simplified profiles, where adjacent points are connected by straight lines, are plotted. On each profile, first point 1 refers to wave arrival; 2-3-4-5-6-7 is the section of the rise to the maximum amplitude, with the points being selected at the inflections of the profiles; and points 8-9-10-11-12 correspond to the descending part. Twelve functions $u_i(h)$ and $t_i(h)$ for each set of five points specify a function of two variables, which is shown above in Fig. 5 (where dashed lines indicate piecewise linear functions ($t_i(h)$)). The choice of points at similar features of the profiles allows us to obtain smoother dependences $u_i(h)$ and $t_i(h)$.

Figure 11 depicts the results of calculating stress and strain diagrams for the profiles of films 480, 580, 740, and 970 nm thick. For the calculation, Eqs. (4) and (5) are numerically integrated using a boundary condition for the function $u(h, t_1(h)) = 0$ along the boundary before arrival of the wave. In other words, the lower limits of integration with respect to the variables h or t for the data $t_1(h)$ or $h_1(t)$ correspond to the points on the lower dashed curve in Fig. 5. In our work, in contrast to [59], discontinuities are not taken into account explicitly in the approximation of the function $u(h, t)$. All points are connected using a piecewise linear interpolation. Functions (4) and (5) are numerically integrated using the Quadpack library [77]. The calculation procedure is implemented in the

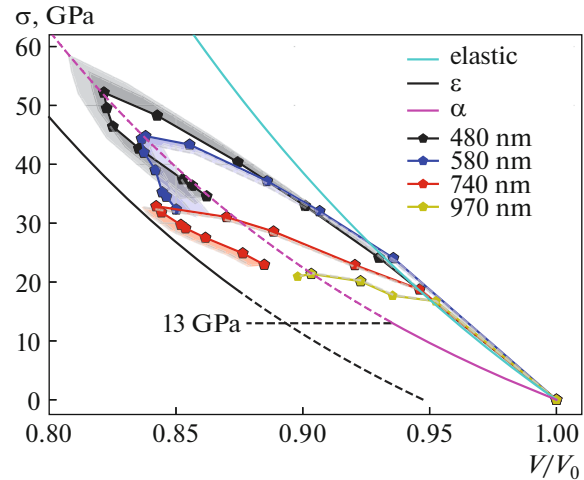


Fig. 11. Calculation of a phase curve by the technique of inverse analysis of kinematic data is shown by points connected by solid lines. The points correspond to the set of reference points from Fig. 4. The shock Hugoniot of various iron phases are shown by solid (in stable phase) and dashed (in metastable phase) lines. The areas of deviation of the trajectories of Lagrangian particles from the corresponding trajectories plotted according to initial experimental data are indicated by color gradation between the corresponding trajectories. The deviations are based on varying film thicknesses of 480 and 580 nm with the corrected time of SW arrival in films with a varied thickness. The pressure of the $\alpha \rightarrow \epsilon$ phase transformation on a sub-microsecond scale is indicated by the black dashed line.

form of interactive Python scripts in the Jupiter environment [78]. Since stress and strain are obtained only in the interpolation region, we are limited to the time of arrival of the elastic wave for the profile of the largest thickness. This time is indicated by the horizontal yellow solid line in Fig. 5. When a σ – V/V_0 diagram is calculated, the last time is approximately 160 ps. Therefore, in particular, the free surface velocity profile in a 970-nm-thick film is only partially calculated.

Thus, Fig. 11 shows the σ – V/V_0 diagram of Lagrangian particles for films 480, 580, 740, and 970 nm thick. The Hugoniot adiabat of the elastic SW is constructed using the points with number 2 on the profiles from Fig. 4. For the first profile, the SW velocity is estimated from the film width and the arrival time; for other films, it is estimated by the ratio of the difference in the film thicknesses to the time difference for the points with the number 2 of the current and previous profiles with a smaller thickness. The shock Hugoniot is specified by a linear dependence of the SW velocity on the substance velocity behind the front ($c_a + s_a u$) and by initial density ρ_0 . For an elastic Hugoniot adiabat, $c_a = 6$ km/s was assumed to be equal to the velocity of sound from [20]. Parameter $s_a = 1.148$ was calculated by the least squares method. Plastic shock Hugoniot are based on the experimental

data [41] with the following set of parameters for the α phase:

$$c_a^\alpha, s_a^\alpha, \rho_0^\alpha = 4.63 \text{ km/s}, \quad 1.33, \quad 7.874 \text{ kg/m}^3,$$

for the ε phase,

$$c_a^\varepsilon, s_a^\varepsilon, \rho_0^\varepsilon = 4.83 \text{ km/s}, \quad 1.33, \quad 8.31 \text{ kg/m}^3.$$

A pressure of 13 GPa marks the boundary of the stable α phase of iron. The solid line in Fig. 11 displays the stable part of the Hugoniot adiabat of the ε phase at high pressures, and the dashed line indicates the metastable phase. The calculation results are investigated to reveal the influence of varying the film thickness and the corresponding SW arrival time.

Figure 11 shows two versions of variation, which are represented by color gradations of the corresponding trajectories of Lagrangian particles in the area of feasible solutions and are limited by gray dashed lines. In the first version, the film thickness is increased from 580 to 600 nm and the corresponding SW arrival time is delayed by 2.3 ps (more saturated color); in the second, in addition to varying a film thickness of 580 nm, a film thickness of 480 nm was decreased to 460 nm, taking into account the earlier wave arrival by 2.3 ps (gray dashes). Both variation and the calculations based on initial data lead to qualitatively identical results.

4. DISCUSSION AND CONCLUSIONS

The $\alpha \rightarrow \varepsilon$ transformation can occur in the region behind the pressure peak in the rarefaction wave, which is partially observed for films 480, 580, and 740 nm thick when the inverse analysis technique is used (see Fig. 11).

In a 480-nm-thick film, a pressure peak is observed in a plastic wave in the α phase of iron. The peak is followed by a rarefaction wave despite the fact that the pressures remain quite high (more than 30 GPa), a partial transformation into the ε phase is detected, and return to the metastable branch of the α phase is noticeable. This phenomenon is unusual, since the reverse transformation pressure decreases to 10 GPa (as compared to 13 GPa in the forward transformation) on unloading from the state of shock compression at 23 GPa [79] or 13 GPa [41] during hydrostatic isothermal compression [49]. The scatter of the stresses and strains related to the variation of the arrival time and the film thickness according to the principle of increasing or decreasing the film thickness by ± 20 nm with the corresponding change in the wave arrival time (± 2.3 ps) weakly affects the phase composition at the pressure peak and at unloading.

A similar initial pattern is observed in a 580-nm-thick film: the pressure reaches its maximum at the Hugoniot adiabat of the α phase. Then, on unloading, partial transformation into the ε phase occurs. The possible scatter of data induced by changes in the film

thickness and the SW arrival time demonstrates both the possibility of continuing the transformation into the ε phase and return to the α phase.

In a 740-nm-thick film, the maximum pressure is reached near the ε phase and unloading leads to a gradual reverse transformation into the α phase of iron. In a 970-nm-thick film, the recorded history is limited to the arrival of SW in a 1160-nm-thick film, which is related to the limited area of stress interpolation using the experimental data obtained by the first measurement of the free surface velocity for an iron film of the largest thickness.

The similar inverse analysis of profiles [21] makes it possible to study the $\alpha \rightarrow \varepsilon$ transformation behind the SW front in a compressed substance at a high strain rate. The difference between this work and [21] is that SW is followed by a rarefaction wave, which promotes a slower phase transformation up to stop and the reverse $\varepsilon \rightarrow \alpha$ transformation; this situation was observed for films 480 and 740 nm thick (see Fig. 11). The behavior is qualitatively reproduced by hybrid mathematical modeling, which provides insight into the heterogeneity and coexistence of various iron phases in compression and rarefaction waves.

ACKNOWLEDGMENTS

We thank K.V. Khishchenko for providing the equations of state of iron and glass and Yu.V. Petrov for the analytical formulas for calculating the electronic properties in transition metals.

FUNDING

This work was supported by the Ministry of Education and Science of the Russian Federation (S.I.A., E.V.S., and P.S.K., state assignment OIVT no. 075-00892-20-00; V.A.Kh. and N.A.I., state assignment ITF no. 00029-2019-0003).

CONFLICT OF INTEREST

The authors declare that they have no conflicts of interest.

REFERENCES

1. S. I. Anisimov, A. M. Prokhorov, and V. E. Fortov, *Izv. Akad. Nauk SSSR, Ser. Fiz.* **46**, 1081 (1982).
2. S. I. Anisimov, A. M. Prokhorov, and V. E. Fortov, *Sov. Phys. Usp.* **27**, 181 (1984).
3. S. I. Anisimov, B. L. Kapeliovich, and T. L. Perel'man, *Sov. Phys. JETP* **39**, 375 (1974).
4. N. A. Inogamov, V. V. Zhakhovskii, C. I. Ashitkov, Yu. V. Petrov, M. B. Agranat, S. I. Anisimov, K. Nishihara, and V. E. Fortov, *J. Exp. Theor. Phys.* **107**, 1 (2008).
5. N. A. Inogamov, V. A. Khokhlov, Yu. V. Petrov, and V. V. Zhakhovskiy, *Opt. Quant. Electron.* **52**, 63 (2020).
6. V. V. Zhakhovskii and N. A. Inogamov, *JETP Lett.* **92**, 521 (2010).

7. N. A. Inogamov, A. M. Oparin, Yu. V. Petrov, et al., *JETP Lett.* **69**, 310 (1999).
8. S. I. Anisimov, V. V. Zhakhovskii, N. A. Inogamov, K. Nishihara, A. M. Oparin, and Yu. V. Petrov, *JETP Lett.* **77**, 606 (2003).
9. R. Fabbro, J. Fournier, P. Ballard, et al., *J. Appl. Phys.* **68**, 775 (1990).
10. N. A. Inogamov, V. A. Khokhlov, and V. V. Zhakhovskii, *JETP Lett.* **108**, 439 (2018).
11. Yu. V. Petrov, N. A. Inogamov, V. V. Zhakhovsky, and V. A. Khokhlov, *Contrib. Plasma Phys.* **59**, e201800180 (2019).
12. C. A. Bolme, S. D. McGrane, D. S. Moore, and D. J. Funk, *J. Appl. Phys.* **102**, 033513 (2007).
13. M. R. Armstrong, J. C. Crowhurst, S. Bastea, and J. M. Zaug, *J. Appl. Phys.* **108**, 023511 (2010).
14. S. I. Ashitkov, M. B. Agranat, G. I. Kanel', P. S. Komarov, and V. E. Fortov, *JETP Lett.* **92**, 516 (2010).
15. V. H. Whitley, S. D. McGrane, D. E. Eakins, et al., *J. Appl. Phys.* **109**, 013505 (2011).
16. J. C. Crowhurst, M. R. Armstrong, K. B. Knight, et al., *Phys. Rev. Lett.* 107144302 (2011).
17. R. F. Smith, J. H. Eggert, R. E. Rudd, et al., *J. Appl. Phys.* **110**, 123515 (2011).
18. G. I. Kanel, *AIP Conf. Proc.* **1426**, 939 (2012).
19. S. I. Ashitkov, M. B. Agranat, G. I. Kanel, and V. E. Fortov, *AIP Conf. Proc.* **1426**, 1081 (2012).
20. S. I. Ashitkov, P. S. Komarov, M. B. Agranat, G. I. Kanel, and V. E. Fortov, *JETP Lett.* **98**, 384 (2013).
21. J. C. Crowhurst, B. W. Reed, M. R. Armstrong, et al., *J. Appl. Phys.* **115**, 113506 (2014).
22. S. I. Ashitkov, P. S. Komarov, E. V. Struleva, M. B. Agranat, and G. I. Kanel, *JETP Lett.* **101**, 276 (2015).
23. V. V. Zhakhovsky, M. M. Budzevich, N. A. Inogamov, et al., *Phys. Rev. Lett.* **107**, 135502 (2011).
24. N. A. Inogamov, V. V. Zhakhovskii, V. A. Khokhlov, and V. V. Shepelev, *JETP Lett.* **93**, 226 (2011).
25. B. J. Demaske, V. V. Zhakhovsky, N. A. Inogamov, and I. I. Oleynik, *Phys. Rev. B* **87**, 054109 (2013).
26. V. V. Zhakhovsky, N. A. Inogamov, B. J. Demaske, et al., *J. Phys.: Conf. Ser.* **500**, 172007 (2014).
27. R. Perriot, V. V. Zhakhovsky, N. A. Inogamov, and I. I. Oleynik, *J. Phys.: Conf. Ser.* **500**, 172008 (2014).
28. K. Khishchenko and A. Mayer, *Int. J. Mech. Sci.* **189**, 105971 (2020).
29. R. Evans, A. D. Badger, F. Fallies, et al., *Phys. Rev. Lett.* **77**, 3359 (1996).
30. K. T. Gahagan, D. S. Moore, D. J. Funk, et al., *Phys. Rev. Lett.* **85**, 3205 (2000).
31. D. J. Funk, D. S. Moore, K. T. Gahagan, et al., *Phys. Rev. B* **64**, 115114 (2001).
32. K. T. Gahagan, D. S. Moore, D. J. Funk, et al., *J. Appl. Phys.* **92**, 3679 (2002).
33. T. Sano, T. Eimura, R. Kashiwabara, et al., *J. Laser Appl.* **29**, 012005 (2017).
34. T. Kawashima, T. Sano, A. Hirose, et al., *J. Mater. Proc. Technol.* **262**, 111 (2018).
35. U. Trdan, T. Sano, D. Klobcar, et al., *Corros. Sci.* **143**, 46 (2018).
36. J. D. G. Greener, E. de Lima Savi, A. V. Akimov, et al., *ACS Nano* **13**, 11530 (2019).
37. Y. Wang, D. H. Hurley, Z. Hua, et al., *Nat. Commun.* **11**, 1597 (2020).
38. E. I. Urazakov and L. A. Fal'kovskii, *Sov. Phys. JETP* **36**, 1214 (1973).
39. V. V. Kosachev, Yu. N. Lokhov, and V. N. Chukov, *Sov. Phys. JETP* **67**, 1825 (1988).
40. Y. Sugawara, O. B. Wright, O. Matsuda, et al., *Phys. Rev. Lett.* **88**, 185504 (2002).
41. S. I. Ashitkov, V. V. Zhakhovsky, N. A. Inogamov, et al., *AIP Conf. Proc.* **1793**, 100035 (2017).
42. V. V. Zhakhovsky, K. P. Migdal, N. A. Inogamov, and S. I. Anisimov, *AIP Conf. Proc.* **1793**, 070003 (2017).
43. G. I. Kanel', V. E. Fortov, and S. V. Razorenov, *Phys. Usp.* **50**, 771 (2007).
44. G. I. Kanel', E. B. Zaretskii, S. V. Razorenov, et al., *Phys. Usp.* **60**, 415 (2017).
45. G. I. Kanel', S. V. Razorenov, G. V. Garkushin, S. I. Ashitkov, P. S. Komarov, and M. B. Agranat, *Phys. Solid State* **56**, 1569 (2014).
46. L. V. Al'tshuler, *Sov. Phys. Usp.* **8**, 52 (1965).
47. G. I. Kerley, Report SAND93-0027 (Sandia Natl. Labor., Albuquerque, 1993).
48. D. Bancroft, E. L. Peterson, and S. Minshall, *J. Appl. Phys.* **27**, 291 (1956).
49. L. M. Barker and R. E. Hollenbach, *J. Appl. Phys.* **45**, 4872 (1974).
50. G. E. Duvall and R. A. Graham, *Rev. Mod. Phys.* **49**, 523 (1977).
51. A. V. Anan'in, A. N. Dremin, and G. I. Kanel', *Fiz. Goreniya Vzryva* **3**, 93 (1981).
52. V. D. Gluzman, G. I. Kanel', V. F. Loskutov, et al., *Probl. Prochn.* **8**, 52 (1985).
53. S. A. Dyachkov, D. K. Ilnitsky, A. N. Parshikov, and V. V. Zhakhovsky, *J. Phys.: Conf. Ser.* **1556**, 012032 (2020).
54. J. P. Geindre, P. Audebert, S. Rebibo, and J. C. Gauthier, *Opt. Lett.* **26**, 1612 (2001).
55. S. Ogata, J. Li, N. Hirosaki, Y. Shibutani, and S. Yip, *Phys. Rev. B* **70**, 104104 (2004).
56. D. M. Clatterbuck, D. C. Chrzan, and J. W. Morris, *Acta Mater.* **51**, 2271 (2003).
57. J. B. Aidun and Y. M. Gupta, *J. Appl. Phys.* **69**, 6998 (1991).
58. J. C. Boettger and D. C. Wallace, *Phys. Rev. B* **55**, 2840 (1997).
59. B. W. Reed, J. S. Stolken, R. W. Minich, and M. Kumar, *J. Appl. Phys.* **110**, 113505 (2011).
60. B. W. Reed, J. Reed Patterson, D. C. Swift, et al., *J. Appl. Phys.* **110**, 113506 (2011).
61. T. Q. Qiu and C. L. Tien, *J. Heat Transfer* **115**, 835 (1993).
62. V. V. Temnov, K. Sokolowski-Tinten, P. Zhou, and D. von der Linde, *J. Opt. Soc. Am. B* **23**, 1954 (2006).
63. N. A. Inogamov, V. V. Zhakhovskii, and V. A. Khokhlov, *J. Exp. Theor. Phys.* **127**, 79 (2018).

64. S. I. Anisimov, V. V. Zhakhovskii, N. A. Inogamov, K. Nishihara, Yu. V. Petrov, and V. A. Khokhlov, *J. Exp. Theor. Phys.* **103**, 183 (2006).
65. N. A. Inogamov, S. I. Anisimov, Yu. V. Petrov, et al., *Proc. SPIE* **7005**, 70052F (2008).
66. S. I. Ashitkov, P. S. Komarov, V. V. Zhakhovsky, et al., *J. Phys.: Conf. Ser.* **774**, 012097 (2016).
67. K. V. Khishchenko, *J. Phys.: Conf. Ser.* **98**, 032023 (2008).
68. K. V. Khishchenko, *J. Phys.: Conf. Ser.* **653**, 012081 (2015).
69. K. V. Khichshenko, *Math. Montisnigri* **XL**, 140 (2017).
70. Yu. Petrov, K. Migdal, N. Inogamov, et al., *Data in Brief* **28**, 104980 (2020).
71. E. D. Palik, *Handbook of Optical Constants of Solids* (Academic, Boston, 1985).
72. P. J. Steinhardt, D. R. Nelson, and M. Ronchetti, *Phys. Rev. B* **28**, 784 (1983).
73. W. Lechner and C. Dellago, *J. Chem. Phys.* **129**, 114707 (2008).
74. C. L. Kelchner, S. J. Plimpton, and J. C. Hamilton, *Phys. Rev. B* **58**, 11085 (1998).
75. B. A. Klumov, S. A. Khrapak, and G. E. Morfill, *Phys. Rev. B* **83**, 184105 (2011).
76. H. Hwang, E. Galtier, H. Cynn, et al., *Sci. Adv.* **6**, eaaz5132 (2020).
77. R. Piessens, E. D. Doncker-Kapenga, C. Ueberhuber, and D. Kahaner, *Quadpack: A Subroutine Package for Automatic Integration* (Springer, Berlin, 2011).
78. Th. Kluyver, B. Ragan-Kelley, F. Pérez, et al., *Positioning and Power in Academic Publishing: Players, Agents and Agendas* (IOS Press, Amsterdam, 2016), p. 87.
79. Th. J. Ahrens, in *Shock Wave Experiments* (Springer, Dordrecht, 2007), p. 912.

Translated by K. Shakhlevich